IEEE Access
Multidisciplinary : Rapid Review : Open Access Journal

Received 9 September 2023, accepted 23 September 2023, date of publication 4 October 2023, date of current version 11 October 2023.

Digital Object Identifier 10.1109/ACCESS.2023.3321651

RESEARCH ARTICLE

Development of a Full Orientation Flight Robotics: Dynamics Modeling, Analysis, and Control Design

YANG-RUI LI AND CHAO-CHUNG PENG, (Member, IEEE)
Department of Aeronautics and Astronautics, National Cheng Kung University, Tainan City 701, Taiwan
Corresponding author: Chao-Chung Peng (ccpeng@mail.ncku.edu.tw)

This work was supported by the Ministry of Science and Technology under Grant MOST 111-2221-E-006-170 and Grant MOST 111-2923-E-006-004-MY3.

ABSTRACT In this paper, a novel multi-rotor flight configuration, namely Full Orientation Flight RObotics (FOFRO), is developed. Different from the well-known quadrotor, the proposed multi-rotor-driven FOFRO is able to achieve arbitrary flight pose in a six-degree-of-freedom (6-DoF) space. Therefore, the demands of flight flexibility and maneuverability can be greatly improved. On the basis of the designed prototype, the 6-DoF governing equations based on quaternion attitude kinematics are derived. Owing to the existence of the multi-rotor-driving redundancy, the optimal control allocation algorithm is further proposed to address the inverse mapping problem between the control signal channels and the actuator driving force channels. The algorithm provides a minimum-energy-consumption solution for a rotor speed to compose the designed control force under the satisfaction of practical physical constraints. To ensure the flight robustness in the realistic scenarios, a robust super-twisting sliding model controller is adopted to against unknown external disturbances. A numerical simulation is performed to illustrate the flight properties of the proposed FOFRO and to validate the feasibility of the proposed optimal control allocation algorithm. Simulation results also reveal that the proposed FOFRO can achieve arbitrary flight pose demands in the 6-DoF space, which demonstrate the high mobility of the proposed FOFRO.

INDEX TERMS Full orientation flight robotics (FOFRO), arbitrary flight pose tracking, optimal control allocation algorithm, robust super-twisting sliding mode controller.

I. INTRODUCTION

In recent years, flight control and the application of UAVs, especially quadrotor helicopters, have become popular research topics. Related studies include tutorial papers [1], [2], [3], robust backstepping sliding mode control [4], [5], [6], linear quadratic regulator control [7], fault-tolerance control [8], [9], path-following control [10], and model predictive control [11], [12]. Compared to traditional quadcopters, tilt-rotor UAVs [13], [14], [15] feature a structure with variable thrust directions, offering increased control versatility. However, UAVs with such variable structure actuation systems pose relatively greater challenges in terms of maintenance. Additionally, most of the existing UAVs rely on changes in orientation to achieve specific trajectory tracking. This limitation raises an interesting question: "Is there a simple configuration for flight robotics that can achieve arbitrary 6-DoF motion control?" As a result, this study proposes a novel multi-rotor-driven UAV, named FOFRO. Unlike the well-known UAVs, the proposed FOFRO can achieve arbitrary 6-DoF motion tracking without relying on changes in attitude.

In regard to the flight dynamic features of a UAV, the governing equations of rotational motion are highly coupled and nonlinear. Moreover, in real flight environments, there exist unavoidable external disturbances. As a result, a robust nonlinear controller design with disturbances rejection should be taken into consideration. Among the several well-known robust control schemes [16], [17], [18], [19], sliding mode control (SMC) techniques have been recognized as an effective and outstanding control algorithm

The associate editor coordinating the review of this manuscript and approving it for publication was Guillermo Valencia-Palomo.

© 2023 The Authors. This work is licensed under a Creative Commons Attribution-NonCommercial-NoDerivatives 4.0 License.
For more information, see https://creativecommons.org/licenses/by-nc-nd/4.0/

[20], [21], [22]. The main reasons include (i) ease of design and implementation (ii) high robustness against model uncertainties, as well as external disturbances, and (iii) fast convergence within finite time. However, the conventional SMC causes difficulty in practical implementation due to the high-frequency chattering effect [20]. In control practices, a trick using extended state information in the sliding surface was presented for chattering reduction [23]. In order to avoid control chattering, second-order sliding mode techniques are adopted in this paper. The relevant technology was first proposed by Levant [24], and the robust control algorithm was later known as the super-twisting algorithm. To address the closed-loop feature of the nonlinear control algorithm, a novel Lyapunov function is presented [25], which provides deep insight into the convergence and robustness properties of the algorithm. For related papers, please refer to [26], [27], [28], and [29]. The super-twisting algorithm has been applied in several studies to prove its control capability, including quadrotor [30], [31], industrial emulator [32], mobile wheeled inverted pendulum [33], spacecraft attitude control [34], and so on.

Control allocation, the mapping of designed control forces to actuator channels, is crucial in various multi-rotor UAV applications. In one study [35], a control allocation scheme utilizing Levy flight-based metaheuristic algorithms is presented for innovative control effector aircraft with integer-constrained actuators. Another study [36] focuses on coordinating thrust vectoring and mass control for flying saucers, employing variable structure control while considering actuator dynamics and aerodynamic coefficient uncertainties to enhance system robustness. Additionally, research [37] addresses control allocation challenges due to linear descriptions and inaccurate efficiency coefficients, introducing an iterative closed-loop configuration and a nonlinear iterative method to reduce allocation errors. In our novel UAV configuration, we propose an optimal control allocation algorithm based on minimizing energy effort while satisfying rotor physical constraints, enhancing the suitability of the considered configuration for real-world control applications.

In this article, a novel UAV flight configuration is proposed so that highly flexible 6-DoF flight trajectories can be achieved. The contributions of this paper are summarized as follows: 1) A novel flight configuration, namely FOFRO, is proposed that is able to track arbitrary 6-DoF motion trajectory. 2) The 6-DoF governing equations based on quaternion representation are derived. 3) An optimal control allocation algorithm is proposed to address the inverse mapping problem from the control force channels to the actuator driving force channels. 4) The quaternion-based feedback control scheme combined with the robust super-twisting sliding mode algorithm is developed. No singularity will be induced for arbitrary flight pose. 5) A Numerical simulation is conducted to illustrate the properties and feasibility of the proposed FOFRO. The results reveal the effectiveness, novelty, and potential applications of the proposed FOFRO.

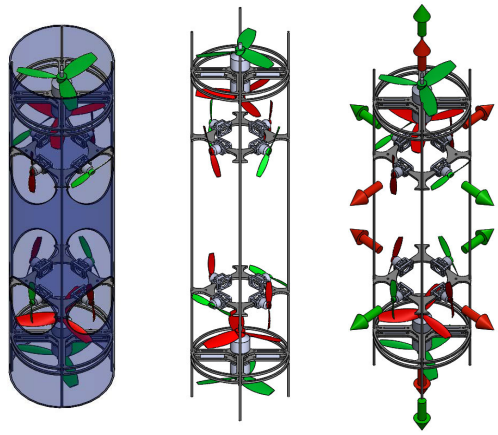

FIGURE 1. The prototype of the proposed FOFRO.

The organization of this paper is described as follows. In Section II, to pursue the feasibility of arbitrary flight trajectories, the quaternion-based governing equations are derived. Furthermore, from the viewpoint of practical control realization, the physical thrust limitation caused by the actuators is accounted for. The force distribution analysis for guaranteeing non-negative rotor speeds was solved in terms of a constrained optimization problem. In Section III, the super-twisting algorithm is adopted to obtain the robust flight controller for trajectory tracking tasks. In Section IV, the strategy of attitude command generation based on the well-known Euler attitude kinematics is presented. In Section V, to avoid discontinuous flight demands, the command prefilters for generating the smooth position, velocity, and acceleration commands from a given position command are applied. In Section VI, a flight numerical simulation is carried out and the simulation results show that the proposed FOFRO can achieve arbitrary 6-DoF motion trajectories. Moreover, with the aid of constrained actuator designs, reasonably generated thrusts can also be realized. Finally, in Section VII, conclusions regarding the simulation results are made.

II. DYNAMICS MODELING AND CONTROL ALLOCATION

In this paper, a novel flight configuration that is able to achieve arbitrary 6-DoF motion is proposed. The prototype can be referred to as Fig. 1. It contains twelve rotors to provide the thrust F_i and the induced torques τ_i, $i = 1, 2, \cdots, 12$, for the trajectory tracking demands. In Fig. 1, the opposite direction of the arrow is the direction of thrust. The green arrow that represents the thrust direction is the same as the rotation direction. The red arrow represents the thrust direction opposite the rotation direction. In what follows, the equations of motion of the proposed FOFRO and the related control allocation analysis are discussed.

A. DYNAMICS MODELING

Based on the prototype of the FOFRO as shown in Fig. 1, the corresponding free body diagram is depicted in Fig. 2. There are two reference frames to be used to describe the motion of

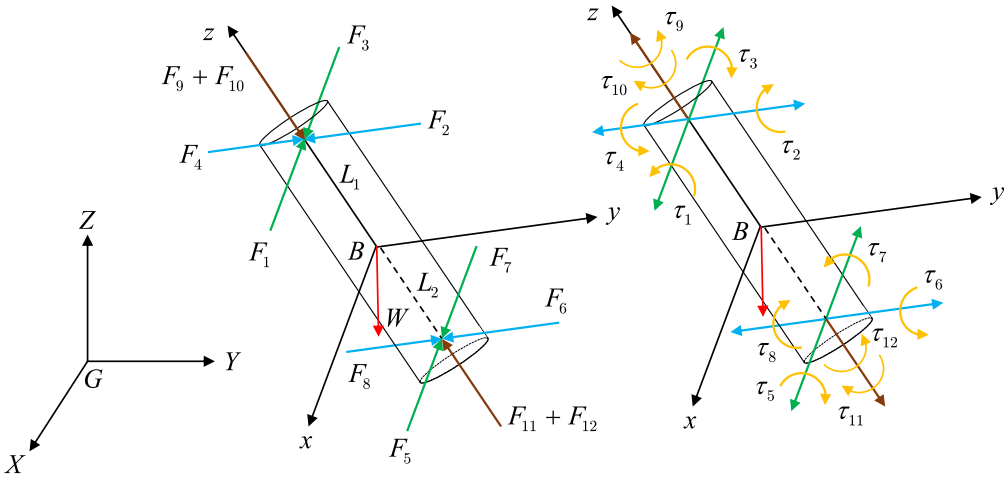

FIGURE 2. Free body diagram of the proposed FOFRO.

the FOFRO. One is the global frame, which is used to describe the absolute motion of the rigid body, represented by $GXYZ$; and the other is the body frame, $Bxyz$, which is fixed in the FOFRO's body to illustrate the relative rotation of the body to the global frame.

To avoid the singularity issue for the control of the FOFRO, the quaternion-based attitude representation is considered. Let $\mathbf{Q} = [q_0, \mathbf{q}^T]^T = [q_0, q_1, q_2, q_3]^T \in \mathbb{R}^4$ be the set of unit quaternion which rotates a vector from the body frame to the global frame. The corresponding direction cosine matrix (DCM) can be constructed by [38]

$$^G\mathbf{C}^B(q_0, \mathbf{q}) = (q_0^2 - \mathbf{q}^T\mathbf{q})\mathbf{I}_3 + 2\mathbf{q}\mathbf{q}^T + 2q_0\mathbf{q}^\times \tag{1}$$

where $\mathbf{I}_3 \in \mathbb{R}^{3\times3}$ is the identity matrix with, and the notation $\mathbf{a}^\times \in \mathbb{R}^{3\times3}$ represents the cross product matrix for a vector $\mathbf{a} = [a_1, a_2, a_3]^T \in \mathbb{R}^3$, defined as follows:

$$\mathbf{a}^\times = \begin{bmatrix} 0 & -a_3 & a_2 \\ a_3 & 0 & -a_1 \\ -a_2 & a_1 & 0 \end{bmatrix} \tag{2}$$

Regarding Fig. 2, denote $\mathbf{F}_a = [F_x, F_y, F_z]^T \in \mathbb{R}^3$ and $\mathbf{M}_a = [M_x, M_y, M_z]^T \in \mathbb{R}^3$ as the resultant force and torque defined in the body frame, respectively. The force $\mathbf{F}_a$ and the torque $\mathbf{M}_a$ are composed of F_i and τ_i, i.e.,

$$\begin{aligned} F_x &= -(F_1 - F_3 + F_5 - F_7) \\ F_y &= -(F_2 - F_4 + F_6 - F_8) \\ F_z &= -(F_9 + F_{10} - F_{11} - F_{12}) \end{aligned} \tag{3}$$

and

$$\begin{aligned} M_x &= \tau_1 - \tau_3 - \tau_5 + \tau_7 \\ &\quad + (F_2 - F_4)L_1 - (F_6 - F_8)L_2 \\ M_y &= -\tau_2 + \tau_4 + \tau_6 - \tau_8 \\ &\quad - (F_1 - F_3)L_1 + (F_5 - F_7)L_2 \\ M_z &= \tau_9 - \tau_{10} - \tau_{11} + \tau_{12} \end{aligned} \tag{4}$$

where L_1 and L_2 are the distances from the top and bottom of the FOFRO to the center of mass B, respectively. Consider the gravitational force $\mathbf{W} \in \mathbb{R}^3$, defined by

$$\mathbf{W} = m\mathbf{g} = \begin{bmatrix} 0 & 0 & -mg \end{bmatrix}^T \tag{5}$$

where m is the mass. To evaluate the flight robustness, further consider the time-varying external disturbances $\mathbf{D}_F \in \mathbb{R}^3$ and $\mathbf{D}_M \in \mathbb{R}^3$, respectively, denoted as

$$\mathbf{D}_F = \begin{bmatrix} D_{F_X} & D_{F_Y} & D_{F_Z} \end{bmatrix}^T \tag{6}$$

$$\mathbf{D}_M = \begin{bmatrix} D_{M_x} & D_{M_y} & D_{M_z} \end{bmatrix}^T \tag{7}$$

Note that (5) and (6) are defined in the global frame, and (7) is defined in the body frame. The governing equations can be easily derived by introducing Newton's second law and Euler's equations of motion to describe the translational and the rotational motions, namely,

$$\mathbf{F}_G = m\ddot{\mathbf{P}} \tag{8}$$

$$\mathbf{M}_G = \left.\frac{d\mathbf{H}_G}{dt}\right)_{body} + \boldsymbol{\omega}^\times\mathbf{H}_G \tag{9}$$

where $\mathbf{F}_G \in \mathbb{R}^3$ and $\mathbf{M}_G \in \mathbb{R}^3$ are the resultant force and torque acting on the center of mass of the rigid body; $\mathbf{P} = [X, Y, Z]^T \in \mathbb{R}^3$ is the absolute position of the rigid body and $\ddot{\mathbf{P}} \in \mathbb{R}^3$ is the associated absolute acceleration; $\mathbf{H}_G \in \mathbb{R}^3$ is the angular momentum; and $\boldsymbol{\omega} = [\omega_x, \omega_y, \omega_z]^T \in \mathbb{R}^3$ is the angular velocity. Both $\mathbf{H}_G$ and $\boldsymbol{\omega}$ are defined in the body frame. Suppose the blades of the rotors are massless, therefore, the overall angular momentum can be simplified as $\mathbf{H}_G = \mathbf{J}\boldsymbol{\omega}$, where $\mathbf{J} \in \mathbb{R}^{3\times3}$ is the moment of inertia matrix of the body. Hence, (9) becomes

$$\mathbf{J}\dot{\boldsymbol{\omega}} + \boldsymbol{\omega}^\times\mathbf{J}\boldsymbol{\omega} = \mathbf{M}_G \tag{10}$$

According to the previous illustration, the $\mathbf{F}_G$ and $\mathbf{M}_G$ can be expressed by

$$\mathbf{F}_G = {}^G\mathbf{C}^B\mathbf{F}_a + \mathbf{W} + \mathbf{D}_F \tag{11}$$

$$\mathbf{M}_G = \mathbf{M}_a + \mathbf{D}_M \tag{12}$$

Note that ${}^G\mathbf{C}^B$ is defined in (1). Refer to the quaternion-based kinematics [39], [40], the governing equations of the

proposed FOFRO can be summarized as follows:

$$m\ddot{\mathbf{P}} = {}^{G}\mathbf{C}^{B}\mathbf{F}_a + \mathbf{W} + \mathbf{D}_F \tag{13}$$

$$\dot{q}_0 = -\frac{1}{2}\mathbf{q}^T\boldsymbol{\omega} \tag{14}$$

$$\dot{\mathbf{q}} = \frac{1}{2}\left(q_0\mathbf{I} + \mathbf{q}^{\times}\right)\boldsymbol{\omega} \tag{15}$$

$$\mathbf{J}\dot{\boldsymbol{\omega}} = \mathbf{M}_a + \mathbf{D}_M - \boldsymbol{\omega}^{\times}\mathbf{J}\boldsymbol{\omega} \tag{16}$$

The control objective is to seek the robust control force $(\mathbf{F}_a, \mathbf{M}_a)$ to drive the system achieve the desired trajectory tracking demands. The control force $(\mathbf{F}_a, \mathbf{M}_a)$ are generated by the multi-rotors configuration as illustrated in Fig. 1. The optimal control allocation algorithm for composing $(\mathbf{F}_a, \mathbf{M}_a)$ is presented in the next section.

B. OPTIMAL CONTROL ALLOCATION ALGORITHM

To establish the mapping relation for $\mathbf{F}_a$ and $\mathbf{M}_a$ with respect to the given rotor speed Ω_i, where $i = 1, 2, \cdots, 12$, consider the following rotor model [1], [41]:

$$F_i = C_T\Omega_i^2, \quad \tau_i = C_M\Omega_i^2, \; i = 1, 2, \cdots, 12 \tag{17}$$

Note that $C_T > 0$ and $C_M > 0$ are the thrust and torque coefficients, respectively. In practical realization, these coefficients can be identified experimentally. In this study, the rotors can only rotate along a fixed direction, i.e., every rotor is not able to generate negative thrust and negative induced torque. This physical constraint will be taken into consideration of the derivation of the optimal control allocation algorithm.

Based on the hardware configuration of the FOFRO, following is going to develop the optimal control allocation algorithm to construct the mapping relation between the control force channel $[F_x, F_y, \cdots, M_z]$ and the actuator driving force channel $[\Omega_1^2, \Omega_2^2, \cdots, \Omega_{12}^2]$. Combining (3), (4), and (17) gives

$$\begin{bmatrix} F_x \\ F_y \\ F_z \\ M_x \\ M_y \\ M_z \end{bmatrix} = \boldsymbol{\Gamma}_0 \begin{bmatrix} \Omega_1^2 \\ \Omega_2^2 \\ \vdots \\ \Omega_{11}^2 \\ \Omega_{12}^2 \end{bmatrix} \tag{18}$$

where the non-square matrix $\boldsymbol{\Gamma}_0 \in \mathbb{R}^{6\times 12}$ related to the C_T, C_M, L_1, and L_2 are

$$\boldsymbol{\Gamma}_0 = \begin{bmatrix} -C_T & 0 & 0 & C_M & -C_TL_1 & 0 \\ 0 & -C_T & 0 & C_TL_1 & -C_M & 0 \\ C_T & 0 & 0 & -C_M & C_TL_1 & 0 \\ 0 & C_T & 0 & -C_TL_1 & C_M & 0 \\ -C_T & 0 & 0 & -C_M & C_TL_2 & 0 \\ 0 & -C_T & 0 & -C_TL_2 & C_M & 0 \\ C_T & 0 & 0 & C_M & -C_TL_2 & 0 \\ 0 & C_T & 0 & C_TL_2 & -C_M & 0 \\ 0 & 0 & -C_T & 0 & 0 & C_M \\ 0 & 0 & -C_T & 0 & 0 & -C_M \\ 0 & 0 & C_T & 0 & 0 & -C_M \\ 0 & 0 & C_T & 0 & 0 & C_M \end{bmatrix}^T \tag{19}$$

Given the designed $\mathbf{F}_a$ and $\mathbf{M}_a$, the corresponding rotor speeds are obtained by the inverse mapping of (18):

$$\begin{bmatrix} \Omega_1^2 \\ \Omega_2^2 \\ \vdots \\ \Omega_{11}^2 \\ \Omega_{12}^2 \end{bmatrix} = \boldsymbol{\Gamma}_0^{\dagger} \begin{bmatrix} F_x \\ F_y \\ F_z \\ M_x \\ M_y \\ M_z \end{bmatrix} \tag{20}$$

where $\boldsymbol{\Gamma}_0^{\dagger} = \left(\boldsymbol{\Gamma}_0^T\boldsymbol{\Gamma}_0\right)^{-1}\boldsymbol{\Gamma}_0^T$ denotes the pseudo-inverse (details should be given) of the matrix $\boldsymbol{\Gamma}_0$, where $\boldsymbol{\Gamma}_0^T\boldsymbol{\Gamma}_0$ is invertible.

Although (20) provides a minimum norm solution of Ω_i^2 for $i = 1, 2, \cdots, 12$. The solution does not guarantee that the non-negative rotor speeds can be obtained from (20). To address this issue, reformulate (18) as

$$\begin{bmatrix} F_x \\ F_y \\ F_z \\ M_x \\ M_y \\ M_z \end{bmatrix} = \boldsymbol{\Gamma} \begin{bmatrix} \Omega_1^2 - \Omega_3^2 \\ \Omega_5^2 - \Omega_7^2 \\ \Omega_2^2 - \Omega_4^2 \\ \Omega_6^2 - \Omega_8^2 \\ \Omega_9^2 - \Omega_{11}^2 \\ \Omega_{10}^2 - \Omega_{12}^2 \end{bmatrix} \tag{21}$$

where the force distribution matrix (FDM) is defined by

$$\boldsymbol{\Gamma} = \begin{bmatrix} -C_T & -C_T & 0 & 0 & 0 & 0 \\ 0 & 0 & -C_T & -C_T & 0 & 0 \\ 0 & 0 & 0 & 0 & -C_T & -C_T \\ C_M & -C_M & C_TL_1 & -C_TL_2 & 0 & 0 \\ -C_TL_1 & C_TL_2 & -C_M & C_M & 0 & 0 \\ 0 & 0 & 0 & 0 & C_M & -C_M \end{bmatrix} \tag{22}$$

It should be noticed that the FDM (22) is a non-singular matrix. On the basis of the given control force $(\mathbf{F}_a, \mathbf{M}_a)$, the corresponding squared rotor speed difference can be acquired by taking the inverse mapping of (21):

$$\begin{bmatrix} \Omega_1^2 - \Omega_3^2 \\ \Omega_5^2 - \Omega_7^2 \\ \Omega_2^2 - \Omega_4^2 \\ \Omega_6^2 - \Omega_8^2 \\ \Omega_9^2 - \Omega_{11}^2 \\ \Omega_{10}^2 - \Omega_{12}^2 \end{bmatrix} = \boldsymbol{\Gamma}^{-1} \begin{bmatrix} F_x \\ F_y \\ F_z \\ M_x \\ M_y \\ M_z \end{bmatrix} \triangleq \begin{bmatrix} c_1 \\ c_2 \\ c_3 \\ c_4 \\ c_5 \\ c_6 \end{bmatrix} \tag{23}$$

Eq. (23) gives a unique solution for $\Omega_j^2 - \Omega_{j+2}^2 = c_k$, $j = 1, 5, 2, 6, 9, 10, k = 1, 2, \cdots, 6$. However, it is necessary to determine Ω_i, $i = 1, 2, \cdots, 12$ explicitly. Meanwhile, the physical constraint $\Omega_i > 0$ should be satisfied. As a reason, the following optimization problem for determining Ω_i is proposed:

$$\begin{aligned} &\text{minimize} \quad \mathcal{L}_j = \Omega_j^2 + \Omega_{j+2}^2 \\ &\text{subject to} \quad \Omega_j^2 - \Omega_{j+2}^2 = c_k, \; \Omega_j \geq 0, \; \Omega_{j+2} \geq 0. \end{aligned} \tag{24}$$

for $j = 1, 5, 2, 6, 9, 10$ and $k = 1, 2, \cdots, 6$. To facilitate understanding, taking the first row of (23), $\Omega_1^2 - \Omega_3^2 = c_1$, as an example, (24) becomes

$$\text{minimize} \quad \mathcal{L}_1 = \Omega_1^2 + \Omega_3^2$$

$$\text{subject to} \quad \Omega_1^2 - \Omega_3^2 = c_1, \ \Omega_1 \geq 0, \ \Omega_3 \geq 0. \tag{25}$$

The optimization problem aims to determine the solution of the minimum-energy-consumption $\mathcal{L}_1$ subject to the control requirement $\Omega_1^2 - \Omega_3^2 = c_1$ together with the physical constraints $\Omega_1, \Omega_3 \geq 0$. Later, it will be proven that the optimal solution of (25) is given by

$$\begin{cases} \Omega_1^* = \sqrt{c_1}, \quad \Omega_3^* = 0, & \text{if} \quad c_1 \geq 0 \\ \Omega_1^* = 0, \quad \Omega_3^* = \sqrt{-c_1}, & \text{if} \quad c_1 < 0 \end{cases} \tag{26}$$

To formally address this problem, define the Hamiltonian $\mathcal{H}$ coming with the Lagrange multipliers λ, μ_1, and μ_2 as follows

$$\mathcal{H} = \Omega_1^2 + \Omega_3^2 + \lambda(\Omega_1^2 - \Omega_3^2 - c_1) + \mu_1(-\Omega_1) + \mu_2(-\Omega_3) \tag{27}$$

where the unknown variables are Ω_1, Ω_3, λ, μ_1, and μ_2. Applying the first-order necessary condition, it follows that

$$\left.\frac{\partial \mathcal{H}}{\partial \Omega_1}\right|_* = 2\Omega_1^* + 2\lambda^*\Omega_1^* - \mu_1^* = 0 \tag{28}$$

$$\left.\frac{\partial \mathcal{H}}{\partial \Omega_3}\right|_* = 2\Omega_3^* - 2\lambda^*\Omega_3^* - \mu_2^* = 0 \tag{29}$$

$$\left.\frac{\partial \mathcal{H}}{\partial \lambda}\right|_* = \Omega_1^{*2} - \Omega_3^{*2} - c_1 = 0 \tag{30}$$

$$\left.\frac{\partial \mathcal{H}}{\partial \mu_1}\right|_* = -\Omega_1^* < 0 \tag{31}$$

$$\left.\frac{\partial \mathcal{H}}{\partial \mu_2}\right|_* = -\Omega_3^* < 0 \tag{32}$$

Let $\mu_1^* = \mu_2^* = 0$. From (28) we get $\lambda^* = -1$. Substituting $\lambda^* = -1$ into (29) results in $\Omega_3^* = 0$. Therefore, $\Omega_1^* = \sqrt{c_1}$, for all $c_1 \geq 0$, which can be obtained from (30). Let $\mu_1^* = \mu_2^* = 0$, from (29), it gives $\lambda^* = 1$ and then one can find $\Omega_1^* = 0$ and $\Omega_3^* = \sqrt{-c_1}$ for all $c_1^* < 0$, eventually.

Next, the optimal solution (26) of the optimization problem (25) will be proven from a geometric perspective, the cost function $\mathcal{L}_1 = \Omega_1^2 + \Omega_3^2$ represents a circle with radius $\sqrt{\mathcal{L}_1}$, and the constrain $\Omega_1^2 - \Omega_3^2 = c_1$ behaves as a hyperbola. The solution can also be verified by nonlinear programming. Fig. 3(a) and 3(b) are the schematic diagram. On the one hand, when $c_1 > 0$, $\Omega_1^2 - \Omega_3^2 = c_1$ represents a symmetric hyperbola with respect to the Ω_3 axis. As seen in Fig. 3(a), the optimal solution is the point of intersection; that is $(\Omega_1^*, \Omega_3^*) = (\sqrt{c_1}, 0)$. Note that the constraints $\Omega_1 > 0$ and $\Omega_3 > 0$ must be satisfied. Thus, the solution $(-\sqrt{c_1}, 0)$ is discarded. On the other hand, when $c_1 < 0$, $\Omega_1^2 - \Omega_3^2 = -c_1$ the solution turns out to be another symmetric hyperbola with respect to the Ω_1 axis. As seen in Fig. 3(b), the optimal solution now becomes $(\Omega_1^*, \Omega_3^*) = (0, \sqrt{-c_1})$.

Similarly, the non-negative rotor speed of the remaining rotors can be obtained in a similar manner. Finally, the optimal control allocation algorithm based on the optimization problem (24) is concluded as follows:

$$\begin{cases} \Omega_j^* = \sqrt{c_k}, \quad \Omega_{j+2}^* = 0, & \text{if} \quad c_k \geq 0 \\ \Omega_j^* = 0, \quad \Omega_{j+2}^* = \sqrt{-c_k}, & \text{if} \quad c_k < 0 \end{cases} \tag{33}$$

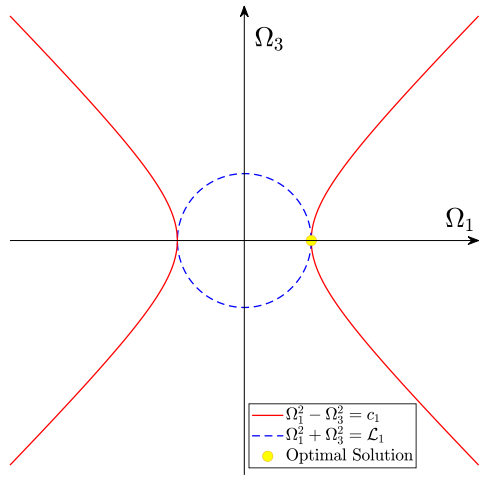

(a) Plot of $\Omega_1^2 + \Omega_3^2 = \mathcal{L}_1$, $\Omega_1^2 - \Omega_3^2 = c_1$, $c_1 > 0$.

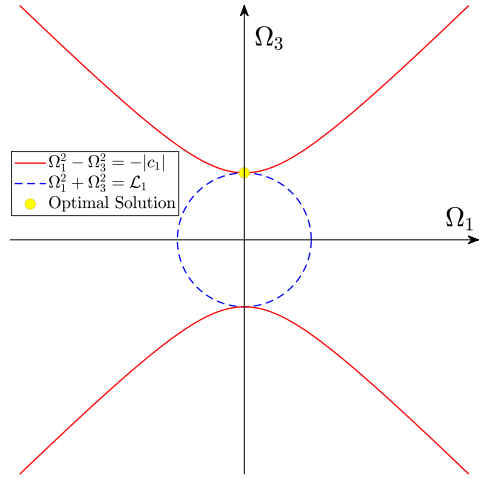

(b) Plot of $\Omega_1^2 + \Omega_3^2 = \mathcal{L}_1$, $\Omega_1^2 - \Omega_3^2 = -|c_1|$, $c_1 < 0$.

FIGURE 3. Solutions of nonlinear programming.

for $j = 1, 5, 2, 6, 9, 10$ and $k = 1, 2, \cdots, 6$.

So far, the governing equations of the proposed FOFRO are derived in (13)–(16). The optimal control allocation algorithm for generated the control force $(\mathbf{F}_a, \mathbf{M}_a)$ is provided in (23) and (33). In what follows, a robust flight controller is designed for the 6-Dof pose tracking demands in the presence of unknown disturbances.

III. FLIGHT CONTROLLER DESIGN

In this section, a robust control law $(\mathbf{F}a, \mathbf{M}a)$ is designed to achieve trajectory tracking in the presence of unknown time-varying disturbances. The trajectory tracking problem is first transformed into an equivalent stabilization problem of the error system. The error system is derived from the difference between the system dynamics and the desired dynamics. Once the error system is obtained, a robust control law is designed to ensure robust performance. In this study, the super-twisting sliding mode algorithm (STSMA) [24] is adopted to address the robust performance issue. The successful applications of STSMA in flight control have been reported in [30], [31], [32], [33], and [34].

A. ATTITUDE CONTROLLER DESIGN

Let $\mathbf{Q}_d = [q_{0d}, \mathbf{q}_d^T]^T \in \mathbb{R}^4$ be the desired quaternion that represents a vector rotation of the desired frame to the global frame, and $\boldsymbol{\omega}_d = [\omega_{xd}, \omega_{yd}, \omega_{zd}]^T \in \mathbb{R}^3$ be the desired angular velocity defined in desired frame. On the basis of quaternion kinematics, they can be related by

$$\dot{\mathbf{Q}}_d = \frac{1}{2}\mathbf{Q}_d \otimes \boldsymbol{\omega}_d \tag{34}$$

Let $\mathbf{Q}_e = [q_{0e}, \mathbf{q}_e^T] \in \mathbb{R}^4$ be the quaternion error between $\mathbf{Q}$ and $\mathbf{Q}_d$. To be more explicit, the quaternion error is a vector rotation from the body frame to the desired frame. By definition, one gives

$$\mathbf{Q} = \mathbf{Q}_d \otimes \mathbf{Q}_e \tag{35}$$

which implies

$$\mathbf{Q}_e = \mathbf{Q}_d^{-1} \otimes \mathbf{Q} \tag{36}$$

where the notation $\otimes$ represents the quaternion multiplication and $\mathbf{Q}_d^{-1}$ is the quaternion inverse of the desired quaternion $\mathbf{Q}_d$. By taking the time derivative of (35) gives

$$\dot{\mathbf{Q}} = \dot{\mathbf{Q}}_d \otimes \mathbf{Q}_e + \mathbf{Q}_d \otimes \dot{\mathbf{Q}}_e \tag{37}$$

It follows that

$$\begin{aligned}\dot{\mathbf{Q}}_e &= \mathbf{Q}_d^{-1} \otimes \left[\dot{\mathbf{Q}} - \dot{\mathbf{Q}}_d \otimes \mathbf{Q}_e\right] \\ &= \mathbf{Q}_d^{-1} \otimes \left[\frac{1}{2}\mathbf{Q} \otimes \boldsymbol{\omega} - \frac{1}{2}\mathbf{Q}_d \otimes \boldsymbol{\omega}_d \otimes \mathbf{Q}_e\right] \\ &= \frac{1}{2}\mathbf{Q}_d^{-1} \otimes \mathbf{Q} \otimes \boldsymbol{\omega} - \frac{1}{2}\boldsymbol{\omega}_d \otimes \mathbf{Q}_e \\ &= \frac{1}{2}\left[\mathbf{Q}_e \otimes \boldsymbol{\omega} - \boldsymbol{\omega}_d \otimes \mathbf{Q}_e\right] \\ &= \frac{1}{2}\mathbf{Q}_e \otimes \left[\boldsymbol{\omega} - \mathbf{Q}_e^{-1} \otimes \boldsymbol{\omega}_d \otimes \mathbf{Q}_e\right]\end{aligned} \tag{38}$$

By defining the angular velocity error as

$$\boldsymbol{\omega}_e = \boldsymbol{\omega} - \mathbf{R}_e^T \boldsymbol{\omega}_d \tag{39}$$

where $\mathbf{R}_e = \mathbf{R}(q_{0e}, \mathbf{q}_e)$. Eq. (38) becomes

$$\dot{\mathbf{Q}}_e = \frac{1}{2}\mathbf{Q}_e \otimes \boldsymbol{\omega}_e \tag{40}$$

Taking the time derivative about (39) gives

$$\begin{aligned}\dot{\boldsymbol{\omega}}_e &= \dot{\boldsymbol{\omega}} - \left(\dot{\mathbf{R}}_e^T \boldsymbol{\omega}_d + \mathbf{R}_e^T \dot{\boldsymbol{\omega}}_d\right) \\ &= \mathbf{J}^{-1}\left(\mathbf{M}_a + \mathbf{D}_M - \boldsymbol{\omega}^\times \mathbf{J}\boldsymbol{\omega}\right) \\ &\quad - \left[\left(\mathbf{R}_e \boldsymbol{\omega}_e^\times\right)^T \boldsymbol{\omega}_d + \mathbf{R}_e^T \dot{\boldsymbol{\omega}}_d\right]\end{aligned} \tag{41}$$

Therefore, based on (40) and (41), the quaternion-based attitude error dynamics is summarized as follows:

$$\dot{q}_{0e} = -\frac{1}{2}\mathbf{q}_e^T \boldsymbol{\omega}_e \tag{42}$$

$$\dot{\mathbf{q}}_e = \frac{1}{2}\left(q_{0e}\mathbf{I}_3 + \mathbf{q}_e^\times\right)\boldsymbol{\omega}_e \tag{43}$$

$$\begin{aligned}\dot{\boldsymbol{\omega}}_e &= \mathbf{J}^{-1}\left[\mathbf{M}_a + \mathbf{D}_M - \boldsymbol{\omega}^\times \mathbf{J}\boldsymbol{\omega}\right] \\ &\quad - \left[\left(\mathbf{R}_e \boldsymbol{\omega}_e^\times\right)^T \boldsymbol{\omega}_d + \mathbf{R}_e^T \dot{\boldsymbol{\omega}}_d\right]\end{aligned} \tag{44}$$

To apply the STSMA, design the sliding vector $\mathbf{S} = [s_1, s_2, s_3]^T \in \mathbb{R}^3$ as follows

$$\mathbf{S} = \boldsymbol{\omega}_e + c\mathbf{q}_e \tag{45}$$

where the sliding gain $c \in \mathbb{R}^1$ is a positive parameter to be designed. Taking the time derivative of (45) along the error dynamics (43) and (44) yields

$$\begin{aligned}\dot{\mathbf{S}} &= \mathbf{J}^{-1}\left[\mathbf{M}_a + \mathbf{D}_M - \boldsymbol{\omega}^\times \mathbf{J}\boldsymbol{\omega}\right] - \left[\left(\mathbf{R}_e \boldsymbol{\omega}_e^\times\right)^T \boldsymbol{\omega}_d + \mathbf{R}_e^T \dot{\boldsymbol{\omega}}_d\right] \\ &\quad + c \cdot \frac{1}{2}\left(q_{0e}\mathbf{I}_3 + \mathbf{q}_e^\times\right)\boldsymbol{\omega}_e\end{aligned} \tag{46}$$

Based on the STSMA [24], design the control law as

$$\begin{aligned}\mathbf{M}_a &= \boldsymbol{\omega}^\times \mathbf{J}\boldsymbol{\omega} + \mathbf{J}\Big[\left(\mathbf{R}_e \boldsymbol{\omega}_e^\times\right)^T \boldsymbol{\omega}_d + \mathbf{R}_e^T \dot{\boldsymbol{\omega}}_d \\ &\quad - \frac{c}{2}\left(q_{0e}\mathbf{I}_3 + \mathbf{q}_e^\times\right)\boldsymbol{\omega}_e + \mathbf{M}_{a,N}\Big] \\ \mathbf{M}_{a,N} &= -\mathbf{K}_1 \frac{\mathbf{S}}{\|\mathbf{S}\|^{1/2}} - \mathbf{K}_2 \int_0^t \operatorname{sgn}(\mathbf{S})\, d\tau\end{aligned} \tag{47}$$

where the control gain matrices are

$$\begin{aligned}\mathbf{K}_1 &= \operatorname{diag}\left(\left[k_{11}\ k_{12}\ k_{13}\right]\right) \\ \mathbf{K}_2 &= \operatorname{diag}\left(\left[k_{21}\ k_{22}\ k_{23}\right]\right)\end{aligned} \tag{48}$$

and $\operatorname{sgn}(\mathbf{S}) \in \mathbb{R}^3$ is defined as

$$\begin{aligned}\operatorname{sgn}(s_i) &= \begin{cases} 1 & \text{if } s_i > 0 \\ -1 & \text{if } s_i < 0 \end{cases} \\ \operatorname{sgn}(s_i) &\in [-1, 1] \quad s_i = 0 \quad (i = 1, 2, 3)\end{aligned} \tag{49}$$

Substituting (47) into (46) gives

$$\dot{\mathbf{S}} = -\mathbf{K}_1 \frac{\mathbf{S}}{\|\mathbf{S}\|^{1/2}} - \mathbf{K}_2 \int_0^t \operatorname{sgn}(\mathbf{S})\, d\tau + \bar{\mathbf{D}}_M \tag{50}$$

where $\bar{\mathbf{D}}_M = \mathbf{J}^{-1}\mathbf{D}_M = [d_1, d_2, d_3]^T \in \mathbb{R}^3$ is the lumped disturbance. It has been proven that the second-order sliding mode can be established within finite time t_f if the control gains satisfy [27], [34]

$$k_{2i} > \rho_i, \quad k_{1i}^2 > 4k_{2i} \tag{51}$$

where $\rho_i = \sup(|d_i|)$, $i = 1, 2, 3$.

Once the system reaches sliding mode, the system dynamics is governed by the following reduced-order dynamics

$$\dot{q}_{0e} = \frac{c}{2}\mathbf{q}_e^T \mathbf{q}_e \tag{52}$$

$$\dot{\mathbf{q}}_e = -\frac{c}{2}q_{0e}\mathbf{q}_e \tag{53}$$

for all $t \geq t_f$. It has been proven in [34] that the analytical solution of $\dot{q}_{0e}$ of the reduced order dynamics (52) is

$$q_{0e}(t) = 1 + \frac{2\left[q_{0e}(t_f) - 1\right]}{q_{0e}(t_f)[e^{c(t-t_f)} - 1] + 1 + e^{c(t-t_f)}} \tag{54}$$

for all $t \geq t_f$. For a positive sliding gain $c > 0$, it implies $q_{0e} \to q_{0d}$ and $\mathbf{q} \to \mathbf{q}_d$ as $t \to \infty$ [34]. The asymptotic stability of the reduced order dynamics (52) and (53) is guaranteed.

B. POSITION CONTROLLER DESIGN

Let $\mathbf{P}_d = [X_d, Y_d, Z_d]^T \in \mathbb{R}^3$ and $\mathbf{V}_d = \dot{\mathbf{P}}_d = [\dot{X}_d, \dot{Y}_d, \dot{Z}_d]^T \in \mathbb{R}^3$ represent desired position and velocity commands, respectively. The corresponding position and velocity tracking errors are $\mathbf{P}_e = \mathbf{P} - \mathbf{P}_d$ and $\mathbf{V}_e = \dot{\mathbf{P}}_e = \dot{\mathbf{P}} - \dot{\mathbf{P}}_d$. Thus the error dynamics are derived by

$$\dot{\mathbf{P}}_e = \mathbf{V}_e$$

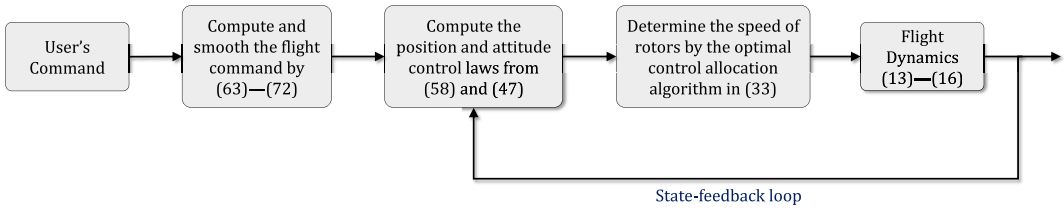

FIGURE 4. Schematic structure of flight control algorithms.

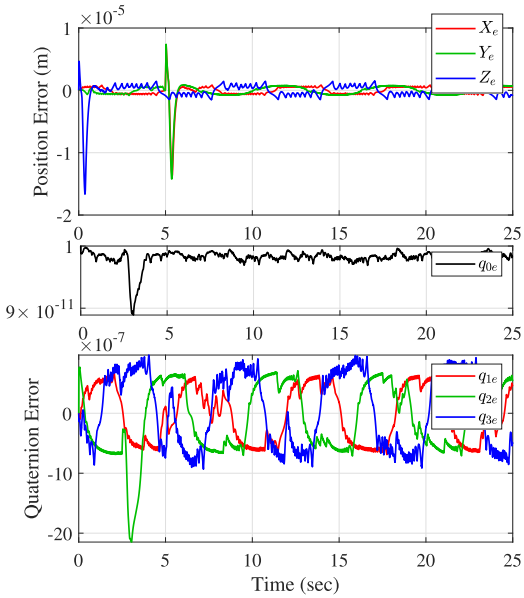

FIGURE 5. Position and quaternion tracking errors.

$$\dot{\mathbf{V}}_e = \frac{1}{m}\left({}^G\mathbf{C}^B\mathbf{F}_a + \mathbf{W} + \mathbf{D}_F\right) - \ddot{\mathbf{P}}_d \tag{55}$$

Design the sliding vector $\mathbf{S}' \in \mathbb{R}^3$ as

$$\mathbf{S}' = \dot{\mathbf{P}}_e + \mathbf{C}\mathbf{P}_e \tag{56}$$

where $\mathbf{C} = \mathrm{diag}\left([c_1, c_2, c_3]\right) > 0 \in \mathbb{R}^{3\times 3}$ is the sliding gain matrix to be designed. Taking the time derivative about (56) gives the sliding dynamics:

$$\dot{\mathbf{S}}' = \frac{1}{m}\left({}^G\mathbf{C}^B\mathbf{F}_a + \mathbf{W} + \mathbf{D}_F\right) - \ddot{\mathbf{P}}_d + \mathbf{C}\dot{\mathbf{P}}_e \tag{57}$$

Based on the STSMA, the control law is designed as

$$\begin{aligned}\mathbf{F}_a &= {}^B\mathbf{C}^G\left[-\mathbf{W} + m\left(\ddot{\mathbf{P}}_d - \mathbf{C}\dot{\mathbf{P}}_e + \mathbf{F}_{a,N}\right)\right]\\ \mathbf{F}_{a,N} &= -\mathbf{K}_1'\frac{\mathbf{S}'}{\|\mathbf{S}'\|^{1/2}} - \mathbf{K}_2'\int_0^t \mathrm{sgn}(\mathbf{S}')\,d\tau\end{aligned} \tag{58}$$

where the control gain matrices are

$$\begin{aligned}\mathbf{K}_1' &= \mathrm{diag}\left(\left[k_{11}'\ k_{12}'\ k_{13}'\right]\right)\\ \mathbf{K}_2' &= \mathrm{diag}\left(\left[k_{21}'\ k_{22}'\ k_{23}'\right]\right)\end{aligned} \tag{59}$$

Substituting (58) into (57) yields

$$\dot{\mathbf{S}}' = -\mathbf{K}_1'\frac{\mathbf{S}'}{\|\mathbf{S}'\|^{1/2}} - \mathbf{K}_2'\int_0^t \mathrm{sgn}(\mathbf{S}')\,d\tau + \bar{\mathbf{D}}_F \tag{60}$$

where $\bar{\mathbf{D}}_F = \frac{1}{m}\mathbf{D}_F = [d_1', d_2', d_3']^T \in \mathbb{R}^3$ represents the lumped disturbance. The finite-time stability can be achieved if the control gains satisfy

$$k_{2i}' > \rho_i', \quad k_{1i}'^2 > 4k_{2i}' \tag{61}$$

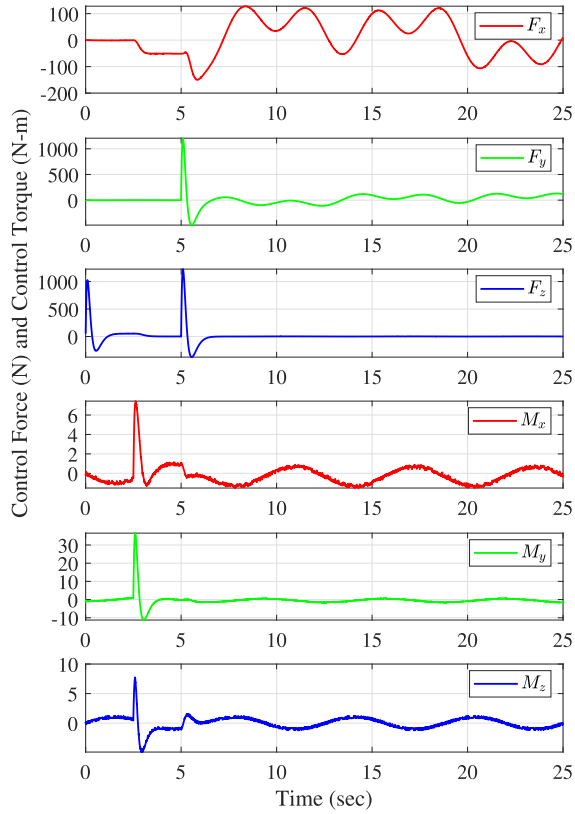

FIGURE 6. Evolution of control force and torque.

where $\rho_i' = \sup(|d_i'|)$, $i = 1, 2, 3$.

Once the sliding motion is fulfilled after a specific time instant t_f', it results in the reduced order dynamics

$$\dot{\mathbf{P}}_e = -\mathbf{C}\mathbf{P}_e \quad \forall t \geq t_f' \tag{62}$$

It is obvious that the asymptotic stability of (62) is guaranteed when $c_i > 0$, $i = 1, 2, 3$.

Because the position dynamics are inherently coupled with the attitude dynamics, the position control law in (58) incorporates feedback information from the DCM. If we were to disregard the DCM, specifically when dealing with small orientation angle approximations, it would be impossible to derive the closed-loop sliding dynamics as shown in (60), along with the corresponding reduced-order system presented in (62).

The position control law (58) is constructed based on a given desired position, velocity, and acceleration commands. The velocity and acceleration commands are obtained by directly taking the derivative for a given position command.

As for the attitude control law (47), the desired quaternion, angular velocity, and angular acceleration should be given. There exist some mathematical operations for attitude command generation. The reference command generation and smoothing strategy are discussed in the next section.

IV. ATTITUDE COMMAND GENERATION

Let $[\phi, \theta, \psi]^T \in \mathbb{R}^3$ be the Euler angle subject to $1 \to 2 \to 3$ convention. Eq. (63) converts the Euler angle to the corresponding quaternion [42]:

$$\begin{bmatrix} q_0 \\ q_1 \\ q_2 \\ q_3 \end{bmatrix} = \begin{bmatrix} c_{\phi/2} \\ 0 \\ 0 \\ s_{\phi/2} \end{bmatrix} \otimes \begin{bmatrix} c_{\theta/2} \\ 0 \\ s_{\theta/2} \\ 0 \end{bmatrix} \otimes \begin{bmatrix} c_{\psi/2} \\ s_{\psi/2} \\ 0 \\ 0 \end{bmatrix} = \begin{bmatrix} c_{\phi/2}\, c_{\psi/2}\, c_{\theta/2} - s_{\phi/2}\, s_{\psi/2}\, s_{\theta/2} \\ c_{\psi/2}\, c_{\theta/2}\, s_{\phi/2} + c_{\phi/2}\, s_{\psi/2}\, s_{\theta/2} \\ c_{\phi/2}\, c_{\psi/2}\, s_{\theta/2} - c_{\theta/2}\, s_{\phi/2}\, s_{\psi/2} \\ c_{\phi/2}\, c_{\theta/2}\, s_{\psi/2} + c_{\psi/2}\, s_{\phi/2}\, s_{\theta/2} \end{bmatrix} \tag{63}$$

where $c_{(\cdot)}$ and $s_{(\cdot)}$ represent $\cos(\cdot)$ and $\sin(\cdot)$, respectively.

According to the Euler-based attitude kinematics, the Euler angle rate $[\dot{\phi}, \dot{\theta}, \dot{\psi}]^T$ related to the angular velocity is described as

$$\begin{bmatrix} \omega_x \\ \omega_y \\ \omega_z \end{bmatrix} = \mathbf{T}(\theta, \psi) \begin{bmatrix} \dot{\phi} \\ \dot{\theta} \\ \dot{\psi} \end{bmatrix} \tag{64}$$

where

$$\mathbf{T}(\theta, \psi) = \begin{bmatrix} c_\psi c_\theta & s_\psi & 0 \\ -c_\theta s_\psi & c_\psi & 0 \\ s_\theta & 0 & 1 \end{bmatrix} \tag{65}$$

Taking the time derivative of (64), it follows that

$$\begin{bmatrix} \dot{\omega}_x \\ \dot{\omega}_y \\ \dot{\omega}_z \end{bmatrix} = \dot{\mathbf{T}}(\theta, \psi, \dot{\theta}, \dot{\psi}) \begin{bmatrix} \dot{\phi} \\ \dot{\theta} \\ \dot{\psi} \end{bmatrix} + \mathbf{T}(\theta, \psi) \begin{bmatrix} \ddot{\phi} \\ \ddot{\theta} \\ \ddot{\psi} \end{bmatrix} \tag{66}$$

where

$$\dot{\mathbf{T}}(\theta, \psi, \dot{\theta}, \dot{\psi}) = \begin{bmatrix} -\dot{\psi} c_\theta s_\psi - \dot{\theta} c_\psi s_\theta & \dot{\psi} c_\psi & 0 \\ \dot{\theta} s_\psi s_\theta - \dot{\psi} c_\psi c_\theta & -\dot{\psi} s_\psi & 0 \\ \dot{\theta} c_\theta & 0 & 0 \end{bmatrix} \tag{67}$$

Therefore, given desired Euler angle $\boldsymbol{\theta}_d = [\phi_d, \theta_d, \psi_d]^T \in \mathbb{R}^3$ and its successive derivatives $[\dot{\phi}_d, \dot{\theta}_d, \dot{\psi}_d]^T \in \mathbb{R}^3$, $[\ddot{\phi}_d, \ddot{\theta}_d, \ddot{\psi}_d]^T \in \mathbb{R}^3$, the attitude command can be generated by introducing (63), (64), and (66):

$$\begin{bmatrix} q_{0d} \\ q_{1d} \\ q_{2d} \\ q_{3d} \end{bmatrix} = \begin{bmatrix} c_{\phi_d/2}\, c_{\psi_d/2}\, c_{\theta_d/2} - s_{\phi_d/2}\, s_{\psi_d/2}\, s_{\theta_d/2} \\ c_{\psi_d/2}\, c_{\theta_d/2}\, s_{\phi_d/2} + c_{\phi_d/2}\, s_{\psi_d/2}\, s_{\theta_d/2} \\ c_{\phi_d/2}\, c_{\psi_d/2}\, s_{\theta_d/2} - c_{\theta_d/2}\, s_{\phi_d/2}\, s_{\psi_d/2} \\ c_{\phi_d/2}\, c_{\theta_d/2}\, s_{\psi_d/2} + c_{\psi_d/2}\, s_{\phi_d/2}\, s_{\theta_d/2} \end{bmatrix} \tag{68}$$

$$\begin{bmatrix} \omega_{xd} \\ \omega_{yd} \\ \omega_{zd} \end{bmatrix} = \mathbf{T}(\theta_d, \psi_d) \begin{bmatrix} \dot{\phi}_d \\ \dot{\theta}_d \\ \dot{\psi}_d \end{bmatrix} \tag{69}$$

$$\begin{bmatrix} \dot{\omega}_{xd} \\ \dot{\omega}_{yd} \\ \dot{\omega}_{zd} \end{bmatrix} = \dot{\mathbf{T}}(\theta_d, \psi_d, \dot{\theta}_d, \dot{\psi}_d) \begin{bmatrix} \dot{\phi}_d \\ \dot{\theta}_d \\ \dot{\psi}_d \end{bmatrix} + \mathbf{T}(\phi_d, \theta_d) \begin{bmatrix} \ddot{\phi}_d \\ \ddot{\theta}_d \\ \ddot{\psi}_d \end{bmatrix} \tag{70}$$

where $\mathbf{T}(\theta_d, \psi_d)$ and $\dot{\mathbf{T}}(\theta_d, \psi_d, \dot{\theta}_d, \dot{\psi}_d)$ are obtained from (65) and (67) by replacing $(\theta, \psi, \dot{\theta}, \dot{\psi})$ with $(\theta_d, \psi_d, \dot{\theta}_d, \dot{\psi}_d)$.

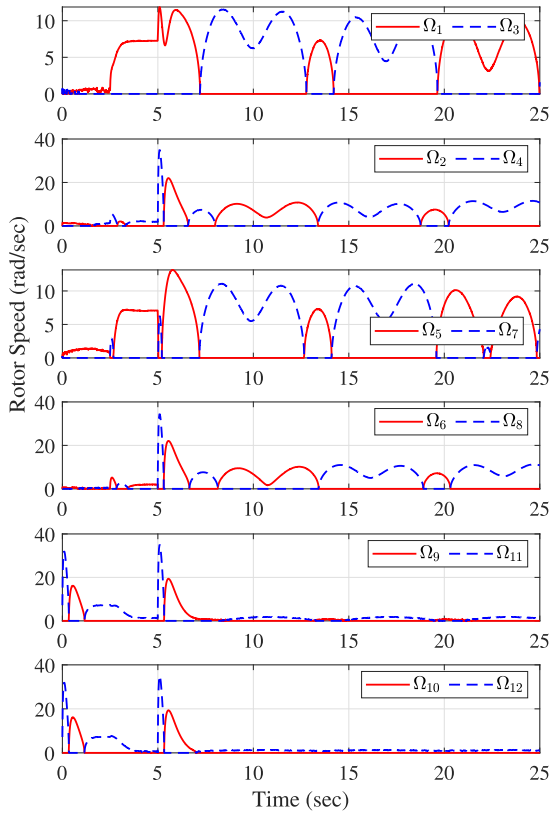

FIGURE 7. Evolution of rotor speed.

V. COMMAND SMOOTHING

For generating the smooth position, velocity, and acceleration commands from a given position command, the following command prefilter is presented:

$$\mathbf{G}(s) = \frac{1}{(\tau s + 1)^p} \begin{bmatrix} 1 \\ s \\ s^2 \end{bmatrix} \tag{71}$$

where p is the order of filter; and $\tau = 1/(2\pi f_c)$, f_c is the associated cut-off frequency (in Hertz). Let $x(s)$ be the original position command, the smooth position command $x_f(s)$, velocity command $v_f(s)$, and acceleration command $a_f(s)$ can be calculated by

$$\begin{bmatrix} x_f(s) \\ v_f(s) \\ a_f(s) \end{bmatrix} = \mathbf{G}(s) x(s) \tag{72}$$

In this study, the position command $\mathbf{P}_d$ and the Euler angle command $\boldsymbol{\theta}_d$ will be given first. The smooth commands are generated from (72) by letting $x(s)$ to be X_d, $Y_d, \cdots, \psi_d$, respectively. Based on (72), the smooth position and the associated velocity, and acceleration commands are obtained. The Euler angle velocity and acceleration commands will be converted to a quaternion, angular velocity, and angular acceleration commands by using (68). As for the design of the filter parameters, a higher filter order, p, and a lower cut-off frequency, f_c, provide more smooth commands. However, it causes an evident phase delay on the command profile. Notice that the filter order p should be greater or equal to 3 for the causality of the filter (72).

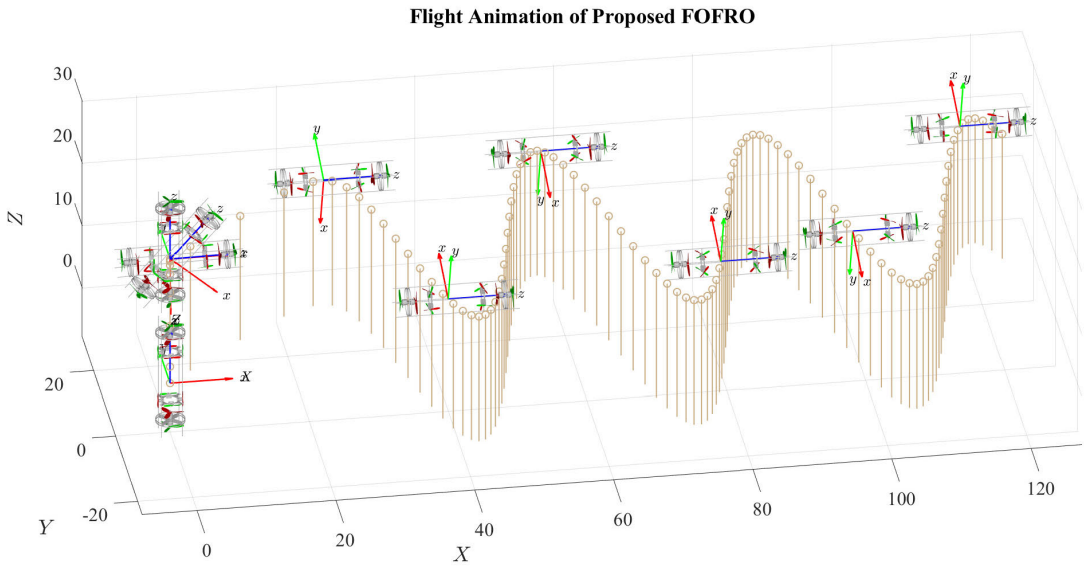

FIGURE 8. The flight pose of the proposed novel FOFRO.

These parameters are designed based on realistic flight scenarios.

To be more comprehensive for the readers to the proposed control algorithms, the schematic structure is depicted in Fig. 4. Moving from left to right in the diagram: 1) The user gives the flight command. 2) By (63)–(72), the smooth flight command is acquired. 3) According to the state-feedback information, realize the position and attitude control laws shown in (58) and (47), respectively. And, 4) Utilizing the optimal control allocation algorithm presented in (33), determine the speed of the rotors to compose the design control force and torque.

VI. NUMERICAL SIMULATION

In the following simulations, the fourth-order Runge-Kutta algorithm with a sampling time of 0.001 second is used. To demonstrate the flight novelty, the following position and Euler angle commands are used:

$$\mathbf{P}_d = \begin{cases} \begin{bmatrix} 0 & 0 & 20 \end{bmatrix}^T & 0 \le t < 5 \\ \begin{bmatrix} 5t & 25\cos(t-5) & 20 \end{bmatrix}^T & 5 \le t \end{cases} \tag{73}$$

$$\boldsymbol{\theta}_d = \begin{cases} \begin{bmatrix} 0 & 0 & 0 \end{bmatrix}^T & 0 \le t < 2.5 \\ \begin{bmatrix} 0 & 0.5\pi & 0 \end{bmatrix} & 2.5 \le t < 5 \\ \begin{bmatrix} 0 & 0.5\pi & 0.25\pi(t-5) \end{bmatrix} & 5 \le t \end{cases} \tag{74}$$

Based on the introduction in Section IV and V, the smooth command is obtained. The cut-off frequency $f_c = 1$ and the order $p = 3$ are used. The system parameters $m = 5.3$, $g = 9.807$, $C_T = 0.5$, $C_M = 0.3$, $L_1 = 0.35$, $L_2 = 0.15$, and

$$\mathbf{J} = \begin{bmatrix} 2.5 & 0.50 & -0.84 \\ 0.50 & 2.5 & 0.52 \\ -0.84 & 0.52 & 1.7 \end{bmatrix} \tag{75}$$

are considered. The initial condition is $\mathbf{P}(0) = [0, 0, 0]^T$, $\dot{\mathbf{P}}(0) = [0, 0, 0]^T$, $q_0(0) = 1$, $\mathbf{q}(0) = [0, 0, 0]^T$, $\boldsymbol{\omega}(0) = [0, 0, 0]^T$. To verify the flight robustness, consider the following disturbance model to simulate the effects of the time-varying disturbances:

$$\begin{aligned} \mathbf{D}_F(t) &= \left[\sin(t)\ \cos(t)\ -\sin(t)\right]^T \\ &\quad + \left[-C_{D_X}\dot{X}\ -C_{D_Y}\dot{Y}\ -C_{D_Z}\dot{Z}\right]^T \\ \mathbf{D}_M(t) &= \left[\sin(t)\ \cos(t)\ -\sin(t)\right]^T \end{aligned} \tag{76}$$

where C_{D_X}, C_{D_Y}, and C_{D_Z} are the drag coefficients. In this paper, $C_{D_X} = 0.25$, $C_{D_Y} = 0.25$, and $C_{D_Z} = 0.75$ are considered. To fulfill the convergent criteria (51) and (61), the control gains $k_{21} = k_{22} = k'_{21} = k'_{22} = 70$, $k_{23} = k'_{23} = 150$, $k_{11} = k_{12} = k'_{11} = k'_{12} = 17.73$, $k_{13} = k'_{13} = 25.49$, and $c = c_1 = c_2 = c_3 = 7$ are applied.

The tracking error of position and quaternion is shown in Fig. 5. The evolution of the control force and the rotor speeds are illustrated in Fig. 6 and Fig. 7, respectively. The observed peak values in Fig. 6 are attributed to discontinuities in commands, as indicated in (73) and (74). Even though in this study, all flight commands are smoothed through a command prefilter, there is always a higher control effort required at the moment of departure from the equilibrium point. The results reveal that the system is able to track the desired command, meanwhile, the reasonable rotors' speed shown in Fig. 7 can be determined to generate the desired control force and the desired torque as shown in Fig. 6. Most importantly, the resultant rotor speeds are realizable from the practical point of view. The detailed flight pose information is visualized in Fig. 8. Simulation firmly confirms the ability of the proposed novel FOFRO for the arbitrary 6-DoF motion tracking demands.

VII. CONCLUSION

In this paper, a novel flight configuration, FOFRO, is proposed and its associated equations of motion are derived.

Simulation results demonstrate that the proposed FOFRO is capable of achieving arbitrary 6-DoF pose tracking tasks without inducing singularity issues. Due to the physical constraints in the FOFRO, it is essential to ensure that each rotor operates at a reasonable speed. Therefore, an optimal control allocation algorithm is proposed to address this problem. Additionally, the STSMA is introduced to guarantee robust performance. The full orientation and high maneuverability of the proposed FOFRO make it applicable to various aerospace engineering problems, such as exploration or rescue missions in particular terrains, material transportation in narrow areas, and so on.

REFERENCES

[1] R. Mahony, V. Kumar, and P. Corke, "Multirotor aerial vehicles: Modeling, estimation, and control of quadrotor," *IEEE Robot. Autom. Mag.*, vol. 19, no. 3, pp. 20–32, Sep. 2012.

[2] A. L'Afflitto, R. B. Anderson, and K. Mohammadi, "An introduction to nonlinear robust control for unmanned quadrotor aircraft: How to design control algorithms for quadrotors using sliding mode control and adaptive control techniques [focus on education]," *IEEE Control Syst. Mag.*, vol. 38, no. 3, pp. 102–121, Jun. 2018.

[3] H. Shraim, A. Awada, and R. Youness, "A survey on quadrotors: Configurations, modeling and identification, control, collision avoidance, fault diagnosis and tolerant control," *IEEE Aerosp. Electron. Syst. Mag.*, vol. 33, no. 7, pp. 14–33, Jul. 2018.

[4] L. Luque-Vega, B. Castillo-Toledo, and A. G. Loukianov, "Robust block second order sliding mode control for a quadrotor," *J. Franklin Inst.*, vol. 349, no. 2, pp. 719–739, Mar. 2012.

[5] F. Chen, R. Jiang, K. Zhang, B. Jiang, and G. Tao, "Robust backstepping sliding-mode control and observer-based fault estimation for a quadrotor UAV," *IEEE Trans. Ind. Electron.*, vol. 63, no. 8, pp. 5044–5056, Aug. 2016.

[6] D. J. Almakhles, "Robust backstepping sliding mode control for a quadrotor trajectory tracking application," *IEEE Access*, vol. 8, pp. 5515–5525, 2020.

[7] M. Faessler, D. Falanga, and D. Scaramuzza, "Thrust mixing, saturation, and body-rate control for accurate aggressive quadrotor flight," *IEEE Robot. Autom. Lett.*, vol. 2, no. 2, pp. 476–482, Apr. 2017.

[8] S. Sun, L. Sijbers, X. Wang, and C. de Visser, "High-speed flight of quadrotor despite loss of single rotor," *IEEE Robot. Autom. Lett.*, vol. 3, no. 4, pp. 3201–3207, Oct. 2018.

[9] Y.-H. Lien, C.-C. Peng, and Y.-H. Chen, "Adaptive observer-based fault detection and fault-tolerant control of quadrotors under rotor failure conditions," *Appl. Sci.*, vol. 10, no. 10, p. 3503, May 2020.

[10] L. Qian and H. H. T. Liu, "Path-following control of a quadrotor UAV with a cable-suspended payload under wind disturbances," *IEEE Trans. Ind. Electron.*, vol. 67, no. 3, pp. 2021–2029, Mar. 2020.

[11] G. Torrente, E. Kaufmann, P. Foehn, and D. Scaramuzza, "Data-driven MPC for quadrotors," 2021, *arXiv:2102.05773*.

[12] L. Bauersfeld, L. Spannagl, G. J. J. Ducard, and C. H. Onder, "MPC flight control for a tilt-rotor VTOL aircraft," *IEEE Trans. Aerosp. Electron. Syst.*, vol. 57, no. 4, pp. 2395–2409, Aug. 2021.

[13] T. Magariyama and S. Abiko, "Seamless 90-degree attitude transition flight of a quad tilt-rotor UAV under full position control," in *Proc. IEEE/ASME Int. Conf. Adv. Intell. Mechatronics (AIM)*, Jul. 2020, pp. 839–844.

[14] K. Liu, L. Ma, H. Zhou, and S. Li, "Structure design and control of a novel tilt-rotor quadrotor with thrust vectoring," in *Proc. IEEE 17th Conf. Ind. Electron. Appl. (ICIEA)*, Dec. 2022, pp. 774–779.

[15] Z.-Y. Lv, Y. Wu, Q. Zhao, and X.-M. Sun, "Design and control of a novel coaxial tilt-rotor UAV," *IEEE Trans. Ind. Electron.*, vol. 69, no. 4, pp. 3810–3821, Apr. 2022.

[16] B. Zhao, B. Xian, Y. Zhang, and X. Zhang, "Nonlinear robust adaptive tracking control of a quadrotor UAV via immersion and invariance methodology," *IEEE Trans. Ind. Electron.*, vol. 62, no. 5, pp. 2891–2902, May 2015.

[17] H. Liu, D. Li, Z. Zuo, and Y. Zhong, "Robust three-loop trajectory tracking control for quadrotors with multiple uncertainties," *IEEE Trans. Ind. Electron.*, vol. 63, no. 4, pp. 2263–2274, Apr. 2016.

[18] S. I. Abdelmaksoud, M. Mailah, and A. M. Abdallah, "Robust intelligent self-tuning active force control of a quadrotor with improved body jerk performance," *IEEE Access*, vol. 8, pp. 150037–150050, 2020.

[19] J. R. S. Benevides, M. A. D. Paiva, P. V. G. Simplício, R. S. Inoue, and M. H. Terra, "Disturbance observer-based robust control of a quadrotor subject to parametric uncertainties and wind disturbance," *IEEE Access*, vol. 10, pp. 7554–7565, 2022.

[20] Y. Shtessel, C. Edwards, L. Fridman, and A. Levant, *Sliding Mode Control and Observation*. Cham, Switzerland: Springer, 2014.

[21] M. Alfayizi, Y. Shtessel, and C. Edwards, "Quad-rotor adaptive sliding mode control using only position and yaw sensors: Generalized relative degree approach," *J. Franklin Inst.*, vol. 359, no. 1, pp. 492–519, Jan. 2022.

[22] J. A. Ricardo Jr. and D. A. Santos, "Smooth second-order sliding mode control for fully actuated multirotor aerial vehicles," *ISA Trans.*, vol. 129, pp. 169–178, Oct. 2022.

[23] L.-H. Chen and C.-C. Peng, "Extended backstepping sliding controller design for chattering attenuation and its application for servo motor control," *Appl. Sci.*, vol. 7, no. 3, p. 220, Feb. 2017.

[24] A. Levant, "Sliding order and sliding accuracy in sliding mode control," *Int. J. Control*, vol. 58, no. 6, pp. 1247–1263, Dec. 1993.

[25] J. A. Moreno and M. Osorio, "A Lyapunov approach to second-order sliding mode controllers and observers," in *Proc. 47th IEEE Conf. Decis. Control*, 2008, pp. 2856–2861.

[26] A. Davila, J. A. Moreno, and L. Fridman, "Optimal Lyapunov function selection for reaching time estimation of super twisting algorithm," in *Proc. 48th IEEE Conf. Decis. Control (CDC) Held Jointly 28th Chin. Control Conf.*, Dec. 2009, pp. 8405–8410.

[27] J. A. Moreno, "A linear framework for the robust stability analysis of a generalized super-twisting algorithm," in *Proc. 6th Int. Conf. Electr. Eng., Comput. Sci. Autom. Control (CCE)*, Jan. 2009, pp. 1–6.

[28] J. A. Moreno and M. Osorio, "Strict Lyapunov functions for the super-twisting algorithm," *IEEE Trans. Autom. Control*, vol. 57, no. 4, pp. 1035–1040, Apr. 2012.

[29] V. Utkin, "On convergence time and disturbance rejection of super-twisting control," *IEEE Trans. Autom. Control*, vol. 58, no. 8, pp. 2013–2017, Aug. 2013.

[30] L. Derafa, A. Benallegue, and L. Fridman, "Super twisting control algorithm for the attitude tracking of a four rotors UAV," *J. Franklin Inst.*, vol. 349, no. 2, pp. 685–699, Mar. 2012.

[31] H. Le Nhu Ngoc Thanh and S. K. Hong, "Quadcopter robust adaptive second order sliding mode control based on PID sliding surface," *IEEE Access*, vol. 6, pp. 66850–66860, 2018.

[32] A. Chalanga, S. Kamal, L. M. Fridman, B. Bandyopadhyay, and J. A. Moreno, "Implementation of super-twisting control: Super-twisting and higher order sliding-mode observer-based approaches," *IEEE Trans. Ind. Electron.*, vol. 63, no. 6, pp. 3677–3685, Jun. 2016.

[33] M. Zhang, J. Huang, and F. Chen, "Super twisting control algorithm for velocity control of mobile wheeled inverted pendulum systems," in *Proc. IEEE Workshop Adv. Robot. Social Impacts (ARSO)*, Sep. 2018, pp. 3–8.

[34] Y.-R. Li and C.-C. Peng, "Super-twisting sliding mode control law design for attitude tracking task of a spacecraft via reaction wheels," *Math. Problems Eng.*, vol. 2021, pp. 1–13, Mar. 2021.

[35] L. Yao, S. You, L. Xiaodong, and G. Bo, "Control allocation for a class of morphing aircraft with integer constraints based on Lévy flight," *J. Syst. Eng. Electron.*, vol. 31, no. 4, pp. 826–840, Aug. 2020.

[36] W. Yinsheng, L. Huazhi, and Z. Youan, "The control allocation of flying saucer with uncertainties," in *Proc. Chin. Control Decis. Conf.*, Jun. 2009, pp. 3402–3405.

[37] Y. Lingyu, Z. Youwu, and S. Gongzhang, "The nonlinear iterative closed loop configuration of control allocation for aircraft with multiple control effectors," in *Proc. Chin. Control Conf.*, Jul. 2007, pp. 755–757.

[38] D. Lee, "Fault-tolerant finite-time controller for attitude tracking of rigid spacecraft using intermediate quaternion," *IEEE Trans. Aerosp. Electron. Syst.*, vol. 57, no. 1, pp. 540–553, Feb. 2021.

[39] H. Abaunza and P. Castillo, "Quadrotor aggressive deployment, using a quaternion-based spherical chattering-free sliding-mode controller," *IEEE Trans. Aerosp. Electron. Syst.*, vol. 56, no. 3, pp. 1979–1991, Jun. 2020.

[40] Y. Wu and G. Yan, "Attitude reconstruction from inertial measurements: QuatFIter and its comparison with RodFIter," *IEEE Trans. Aerosp. Electron. Syst.*, vol. 55, no. 6, pp. 3629–3639, Dec. 2019.

[41] C.-C. Peng and Y.-I. Lin, "Dynamics modeling and parameter identification of a cooling fan system," in *Proc. IEEE Int. Conf. Adv. Manuf. (ICAM)*, Nov. 2018, pp. 257–260.

[42] J.-H. Kim, S.-S. Park, K.-K. Park, and C.-K. Ryoo, "Quaternion based three-dimensional impact angle control guidance law," *IEEE Trans. Aerosp. Electron. Syst.*, vol. 57, no. 4, pp. 2311–2323, Aug. 2021.

YANG-RUI LI was born in Taipei, Taiwan, in 1995. He received the M.S. degree from the Department of Aeronautics and Astronautics (DAA), National Cheng Kung University (NCKU), Tainan, Taiwan, in 2021, where he is currently pursuing the Ph.D. degree with DAA.

His research interests include system dynamics modeling, analysis, identification, state estimation, and control law design/realization for dynamical systems.

CHAO-CHUNG PENG (Member, IEEE) was born in Kaohsiung, Taiwan, in 1980. He received the B.S. degree from the Department of Aeronautics and Astronautics (DAA), National Cheng Kung University (NCKU), Tainan, Taiwan, in 2003, and the Ph.D. degree, in 2009.

From 2008 to 2009, he was a Research Assistant with the Department of Engineering, Leicester University, U.K. From 2010 to 2012, he was a Postdoctoral Fellow with the Department of Mechanical Engineering, NCKU. He was a Senior Engineer with the Embedded System Development Section, Measurement and Automation Department, ADLINK Technology, Taipei, Taiwan, in 2012. From 2014 to 2016, he was with the Iron & Steel Research and Development Department, Automation and Instrumentation System Development Section, China Steel Corporation (CSC), Kaohsiung, Taiwan. Since 2016, he has been an Assistant Professor with the Department of Aeronautics and Astronautics, NCKU. He was promoted as an Associate Professor and a Professor, in 2020 and 2023, respectively. His research interests include high-performance motion control and applications, unmanned vehicle design, advanced flight control system development, autonomous robotics, intelligence simultaneous localization and mapping (SLAM) technology, system modeling, and online diagnosis. He was awarded a membership in the Phi Tau Phi Scholastic Honor Society, in 2009, the Excellent Young Engineering Professor Award by the Chinese Society of Mechanical Engineers (CSME), in 2019, and the Rising Star Award from the College of Engineering, NCKU, in 2023.